Supporting Information for:

Multimodal Nanoscale Mapping of Local Structure and CO_2 Adsorption in Metal–Organic Frameworks

Sarah L. Karstens[1,2], Matthew N. Dods[2,3], Ambarneil Saha[4], Máté Garai[5], William Dai[6], Katerina I. Graf[1], Ryan A. Klein[1,2,7,], Henry Z.H. Jiang[1,2,6], Jung Cho[8], Karen C. Bustillo[4], Markus B. Raschke[5], Peter Ercius[4], Jeffrey R. Long[1,2,3,6], Andrew M. Minor[4,6]

[1]Department of Chemistry, University of California, Berkeley, CA 94720, USA

[2]Institute for Decarbonization Materials, University of California, Berkeley, CA 94720, USA

[3]Department of Chemical and Biomolecular Engineering, University of California, Berkeley, CA 94720, USA

[4]National Center for Electron Microscopy, Molecular Foundry, Lawrence Berkeley National Laboratory, Berkeley, CA 94720, USA

[5]Department of Physics and JILA, University of Colorado, Boulder, CO 80302, USA

[6]Department of Materials Science and Engineering, University of California, Berkeley, CA 94720, USA

[7]Center for Neutron Research, National Institute of Standards and Technology, Gaithersburg, MD 20878, USA

[8]California NanoSystems Institute, University of California, Los Angeles, CA 90095, USA

Table of Contents

1. Materials and Methods

1.1. Pawley Fitting. The data were analyzed using the TOPAS Academic v6 software package.[1] Sequential Pawley fits of the powder patterns were performed to extract the lattice parameter for CO_2-dosed pn–Mg_2(dobpdc) as a function of temperature.[2] 3D ED measurements indicate that the material crystallizes in space group $P3_121$ (space group 152), and we used the lattice parameters and space group found from the electron diffraction measurements to initialize the Pawley fits.

Interestingly, the electron microscopy data indicate a distribution of unit cell sizes in $a = b$. In the PXRD patterns, we observed *hkl*-dependent peak broadening in all collected patterns, where peaks with $l = 0$ were considerably broader than peaks where $l \neq 0$, consistent with the electron microscopy results. A model for the line shape using convolved Lorentzian and Gaussian size and strain parameters did not accurately model the observed *hkl*-dependent peak broadening (Figure S7a). Similar peak broadening has been observed before for mmen-Mn_2(dobpdc), and there the authors used a Stephens model to account for the broadening.[3] Likewise, a Stephens model for peak broadening in a trigonal unit cell was applied in this work.[4] The broadness of the peaks with $l \neq 0$ is much better captured using the Stephens parameters (Figure S7b). The model uses the parameter ζ to convolve Gaussian and Lorentzian shapes and the parameters S_{004}, S_{400}, and S_{202} as the anisotropic strain parameters for the trigonal crystal system. For the Pawley fits, we fixed ζ at 1 and S_{004} at 0 and allowed S_{400} and S_{202} to vary freely. ζ was set to a value of 1 (i.e. pure Lorentzian line shapes) because we observed in the correlation matrix that ζ was highly correlated with other terms. Fixing ζ to 1 did not have an appreciable effect on the fit statistics. In addition, S_{004} was fixed at 0 due to the absence of peaks with $h,k = 0$ and $l \neq 0$ in the pattern. S_{400} and S_{202} were freely refined (Figures S9b and c).[4] Visual inspection of the data as a function of temperature revealed that the peak broadening was also dependent on temperature in the as measured material – during the heating and cooling process, the peaks with $l = 0$ were observed to broaden significantly whereas there was little change observed by eye for the Bragg peaks with $l \neq 0$ (Figure S9a). Therefore, during the sequential Pawley fitting, the lattice parameters a and c and peak shape terms S_{400} and S_{202} were refined. The background was modeled using a shifted Chebyshev polynomial function which was also refined during the sequential fitting. The instrument correction terms for axial divergence and specimen displacement were determined from an initial Pawley fit of the data collected for 360 s at 298 K and then fixed during the sequential fitting process. We observed that the parameter S_{400}, which applies for peaks $h,k \neq 0$ and $l = 0$, increases upon heating to 373 K, then decreases and reaches a constant value after sample activation (Figure S10b). In comparison, the parameter S_{202}, which applies for peaks when $h,k,l \neq 0$, has a smaller change with temperature (Figure S10c).

The results for the sequential Pawley fitting are illustrated in Figure S10 for the two trigonal lattice parameters and the unit cell volume. Upon evacuation at 298 K for 30 min, the lattice parameter a decreased from 21.3974(8) Å to 21.2967(2) Å, while c expanded from 6.8081(2) Å to 6.8485(2) Å. During heating, at approximately 340 K, there was an inflection point in the change in the lattice

parameter *a* with temperature, while *c* expanded monotonically to ca. 350 K and then plateaued, indicating a structural transformation (a higher data density with temperature may yield further insight). After activating at 373 K for 1 h, *a* expanded to 21.4352(19) Å, indicating a second distinct structural transformation. While activating at 373 K, the lattice parameter *c* increased slightly to 6.9539(4) Å after 5 min, then decreased to a value of 6.9418(3) Å. Upon cooling, there was a small contraction in *a*, returning to the same value as in the CO_2-dosed pn–Mg_2(dobpdc) sample (Figure S10a). This could potentially indicate a return to the same crystal structure measured before exposing the sample to dynamic vacuum and before heating. However, the lattice parameter *c* remained relatively stable while cooling, reaching a value of 6.9409(2) Å, ≈ 0.1 Å larger than in CO_2-dosed pn–Mg_2(dobpdc) (Figure S10b). The overall unit cell volume increases significantly upon activation and desorption, from 2690.08(12) $Å^3$ when dosed with CO_2 to 2751.82(7) $Å^3$ after activation (Figure S10c). The thermal expansion coefficient for the unit cell volume found for the material as measured upon cooling is $\alpha = \frac{1}{V}\frac{dV}{dT} = 5.3 \times 10^{-5}\ K^{-1}$ from 373 to 298 K under dynamic vacuum.[5] The somewhat modest linear volumetric thermal expansion over this range is driven almost completely by positive thermal expansion in the *a* axis ($2.6 \times 10^{-5}\ K^{-1}$), which is significantly larger than the minimal thermal expansion observed in the *c* axis ($6.8 \times 10^{-7}\ K^{-1}$). Therefore, we concluded that, even though the final measured *a* lattice parameter recovered to nearly the same value determined before heating, the starting and ending states at 298 K are chemically distinct.

1.2 Structural Elucidation from 3D ED. A single 74.9% complete movie (Dataset 1), which was from a separate data collection session of pn–CO_2–Mg_2(dobpdc) at higher resolution but with otherwise identical collection parameters to the *in situ* session, was sufficient to generate a viable *ab initio* solution at 1.0 Å resolution using SHELXT. Model-building into the *ab initio* electrostatic potential map and subsequent least-squares refinement were conducted in Olex2 using neutral electron scattering factors parameterized into four Gaussian functions. Given the lack of sub-angstrom resolution, all ADPs were refined isotropically, and precision in bond lengths was limited.

Initial refinement of the atomic model was conducted without any geometric constraints or restraints to avoid injecting preconceived bias (overfitting). However, electrostatic potential corresponding to a single carbon atom in the 4,4′-dioxidobiphenyl-3,3′-dicarboxylate linker was visible only at a relatively low contour level of +1.5σ in the $2F_{obs}–F_{calc}$ map (Figure S4), possibly due to lack of completeness. All other non-hydrogen atoms were visible at +3σ (Figure S5). This led to distorted phenyl rings when refined freely. Thus, standard geometric restraints (DFIX, FLAT, SADI) were applied to the carbon atoms in the phenyl ring, and hydrogen atoms were assigned using the riding model. All other atoms were allowed to refine freely. This led to a more chemically reasonable model, albeit with an expectedly high *B*-factor on the problematic carbon atom. The SQUEEZE algorithm was used to account for residual electrostatic potential within the pores of the MOF. Refinement *R*-factors converged to values comparable to published 3D ED structures of MOFs[6,7] (R_1 = 16.26, wR_2 = 45.88, GooF = 1.266, Data/restraints/parameters = 1128/22/46).

Relevant data files and more detailed descriptions of the refinement can be found at https://doi.org/10.5281/zenodo.18111738.

2. Supporting Electron Diffraction Data

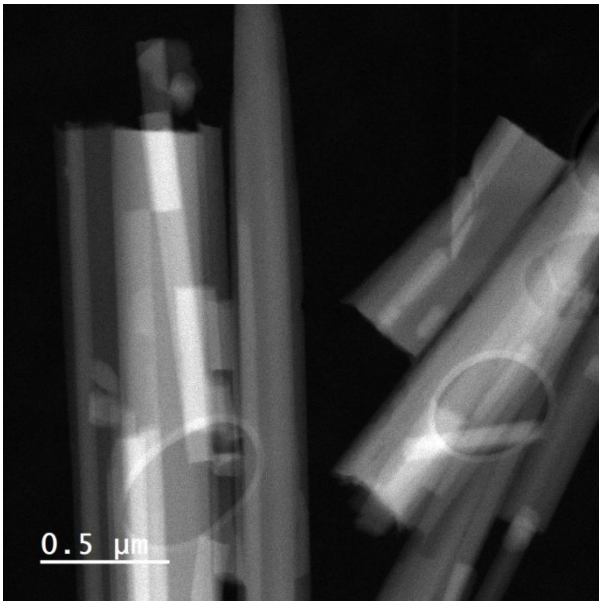

Figure S1. High-angle annular dark field (HAADF) STEM of a cluster of pn–CO_2–Mg_2(dobpdc) crystals. Crystals vary in size, from a few hundred nanometers to over a micron in length. Several crystals overlap along the projection direction.

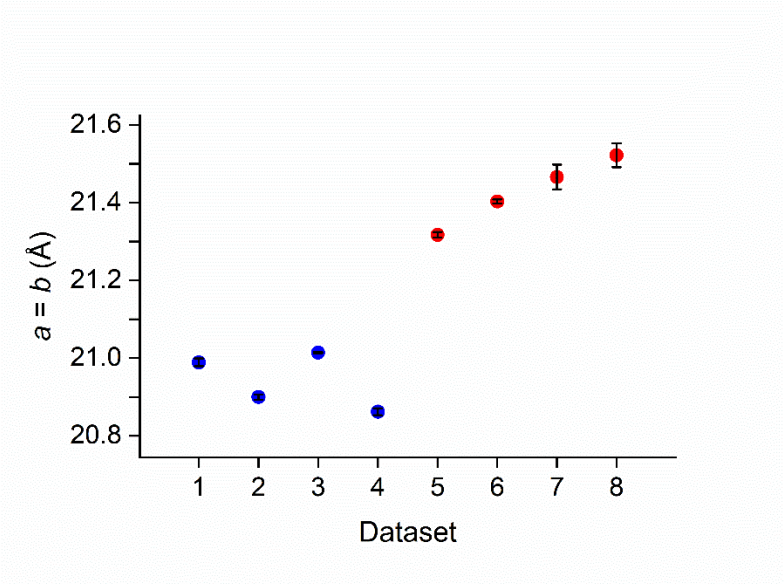

Figure S2. Variation in $a = b$ lattice parameters between different crystals in 3D ED measurement. Blue and red represent before and after *in situ* heating, (i.e. CO_2-dosed and activated phases), respectively. With the exception of Dataset 1, which was used solely for the electrostatic potential map, all datasets were taken during the same session and contribute equally to the averaged results shown in Table 1 of the main text (Dataset 1 does not contribute). Error bars denote estimated standard deviation (ESD) of each crystal's lattice parameter (extracted from XDS).

Table S1. Lattice parameters for diamine-appended Mg_2(dobpdc) derived from 3D electron diffraction (this work) compared to previous computational and experimental values (unit: Å). All structures have the hexagonal crystal structure ($\alpha = \beta = 90°$, $\gamma = 120°$). Across the different diamine-appended frameworks, there is no consistent trend of unit cell expansion or contraction upon CO_2 adsorption.

Diamine		**3D electron diffraction[a]**		**Powder X-ray diffraction[a]**		**Density functional theory**	
		Activated	**CO_2-dosed**	**Activated**	**CO_2-dosed**	**Activated**	**CO_2-dosed**
1,3-	$a = b$	21.427(23)	20.925(30)	21.3958(2)	21.2967(2)	21.554,[8] –	20.688,[8] 21.028[9]
diaminopropane	c	6.862(40)	6.914(7)	6.9409(2)	6.8485(2)	6.794,[8] –	7.056,[8] 7.051[9]
N, N'-	$a = b$	–	–	–	–	21.074[10]	21.498[10]
dimethylethylenediamine	c	–	–	–	–	6.672[10]	7.005[10]
2,2-dimethyl-1,3-	$a = b$	–	–	21.526(2)[9]	21.505(6)[9]	–	–
propanediamine	c	–	–	6.9288(6)[9]	6.9124(14)[9]	–	–
2-	$a = b$	–	–	21.580(2)[11]	21.673(1)[11]	–	–
(aminomethyl)piperidine	c	–	–	6.9289(5)[11]	6.8145(4)[11]	–	–
N, N'-	$a = b$	–	–	21.6248(1)[12]	21.264(2)[12]	–	–
diethylethylenediamine	c	–	–	6.9188(3)[12]	7.0289(5)[12]	–	–

[a]The method to calculate error and precision in lattice parameter determination is very different in 3D ED and PXRD and therefore should not be compared.

Table S2. Compiled statistics for each 3D ED Dataset. With the exception of Dataset 1, which was used solely for the electrostatic potential map, all datasets were taken during the same *in situ* session and contribute equally to the averaged results shown in Table 1 of the main text (Dataset 1 does not contribute).

Dataset Number	**Resolution limit**	**Completeness of data**	R_{merge}	I/σ	R_{meas}	$CC_{(1/2)}$
1	1.0	74.9%	14.9%	3.9	25.9%	99.2
2	1.3	21.1%	4.1%	34.47	5.3%	99.7
3	1.3	47.2%	20.4%	4.60	23.5%	89.5
4	1.3	38.3%	10.0%	10.8	11.4%	97.8
5	1.3	36.6%	6.7%	13.49	8.0%	98.3
6	1.3	55.9%	18.8%	5.83	22.1%	94.3
7	1.3	39.6%	18.3%	4.60	21.4%	96.1
8	1.3	10.0%	8.7%	11.31	9.9%	98.1

Table S3. Data reduction statistics for electron diffraction Dataset 1, used to create the electrostatic potential map in Figure 4. Dataset 1 was taken in a separate session without *in situ* heating (i.e. in the CO_2-dosed phase) and was used solely for the electrostatic potential map. Because it was not taken during the *in situ* session with the other seven datasets, it did not contribute to the averaged results shown in Table 1.

	pn–CO_2–Mg_2(dobpdc)
Temperature (K)	295
Crystal system	Trigonal
Space group	$P3_121$
Point group	32
Laue symmetry	$\bar{3}m$
Unit cell lengths *a*, *b*, *c* (Å)	20.9900(16), 20.9900(16), 7.000(3)[a]
Unit cell angles α, β, γ (°)	90, 90, 120
Unit cell volume (Å^3)	2670.9(12)
Z	1
Radiation source, wavelength (Å)	Transmission electron microscope, 0.0197
Resolution (Å)	1.0
Measured reflections	2140
Unique reflections	1128
Completeness (%)	74.9
$CC_{1/2}$	99.2
R_{int}	14.35%
I/σ	3.9
Index ranges (*h*, *k*, *l*)	17, 10, 6

[a]This data was derived solely from Dataset 1 (Fig. S2) and therefore the determined parameters are slightly different than those in Table S1.

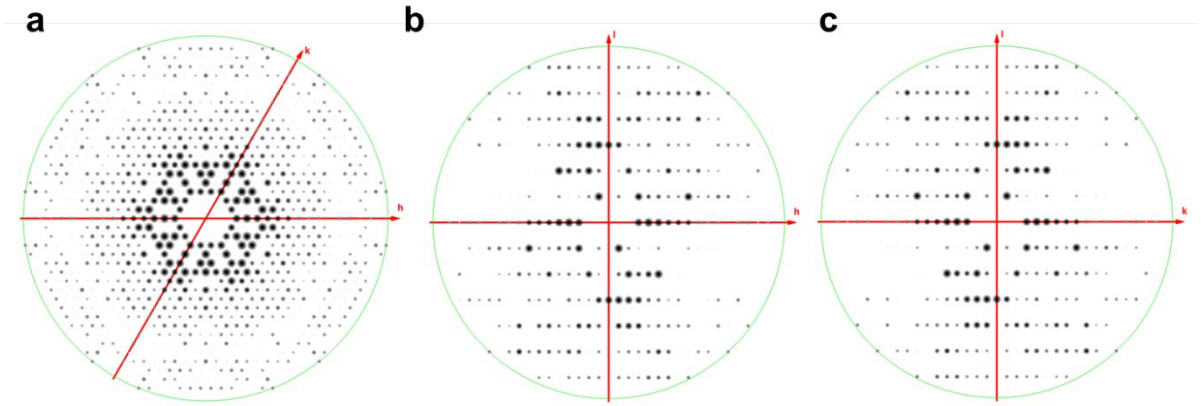

Figure S3. Zones of reciprocal space reconstructed using intensities from Dataset 1: (a) hk0, (b) h0l, and (c) and 0kl planes of pn–CO_2–Mg_2(dobpdc). Blank areas in (b) and (c) represent sections of the reciprocal lattice unsampled in the dataset.

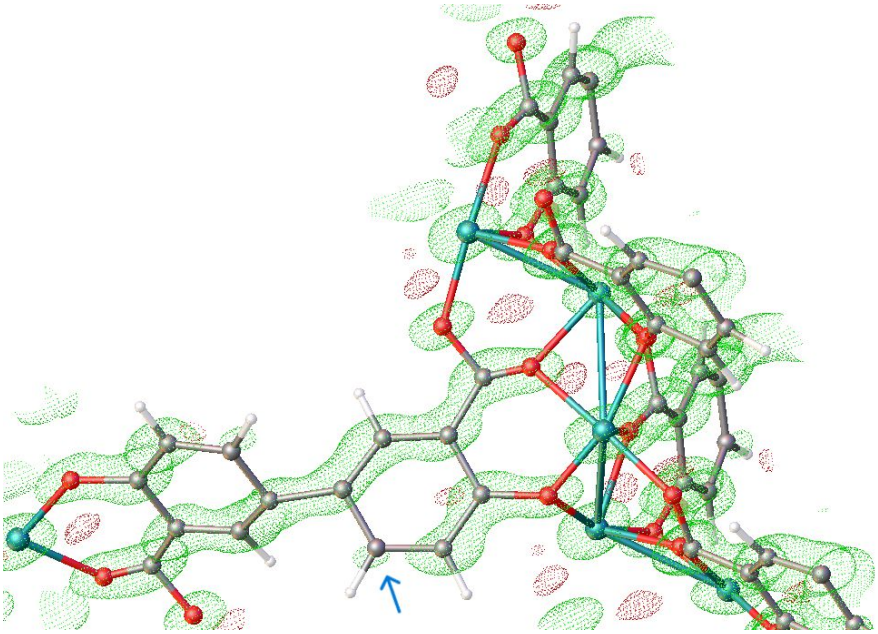

Figure S4. *Ab initio* 1.0-Å resolution weighted electrostatic potential map ($2F_{obs}–F_{calc}$) contoured at +1.5σ, with the refined atomic model superimposed. Carbon atoms are rendered in gray, oxygen atoms in red, magnesium atoms in blue, and hydrogen atoms in white. The blue arrow indicates the problematic carbon atom.

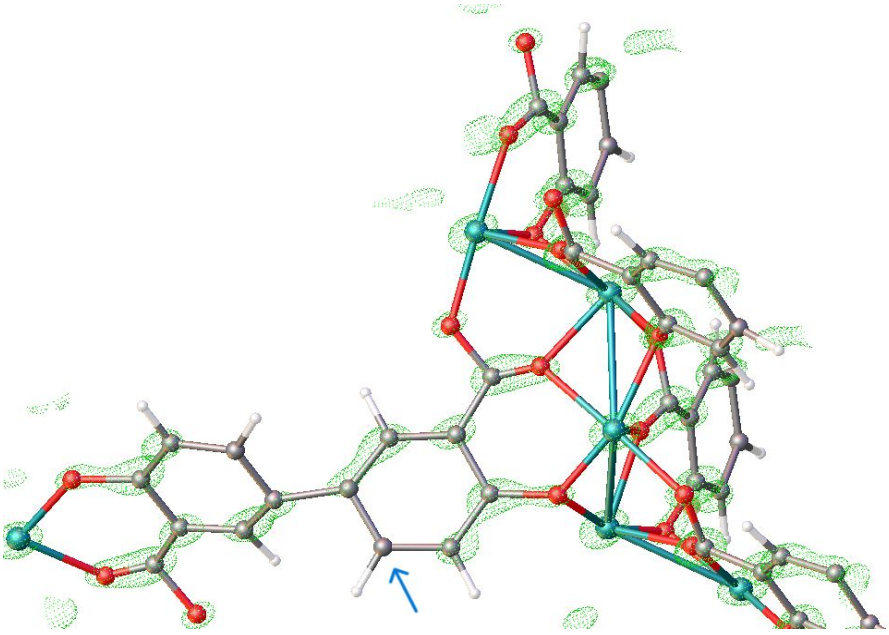

Figure S5. *Ab initio* 1.0-Å resolution weighted electrostatic potential map ($2F_{obs}–F_{calc}$) contoured at +3σ, with the refined atomic model superimposed. Carbon atoms are rendered in gray, oxygen atoms in red, magnesium atoms in blue, and hydrogen atoms in white. The blue arrow indicates the problematic carbon atom.

3. Supporting X-ray Diffraction Data

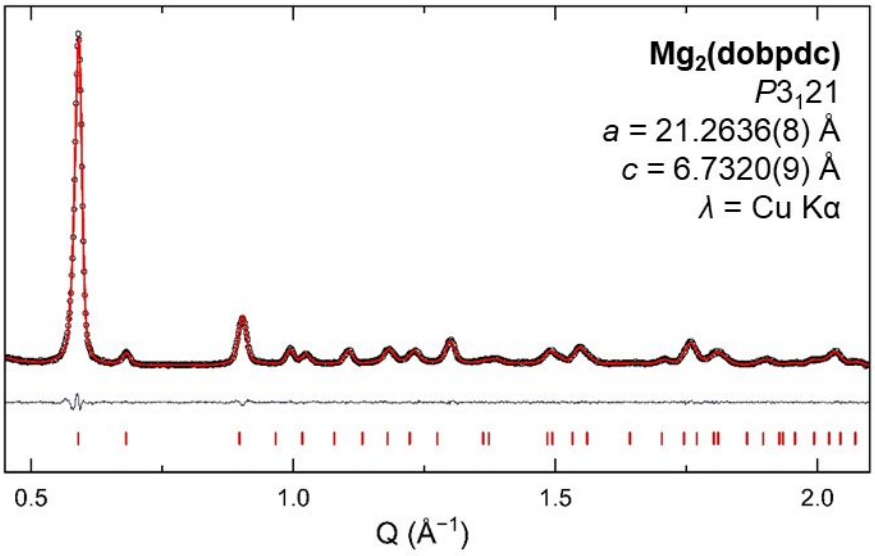

Figure S6. Pawley fit of the powder X-ray diffraction pattern (λ = Cu Kα) for as-synthesized Mg_2(dobpdc) activated and analyzed under air, R_{wp} = 4.531 %, R_p = 3.503 %, R_{exp} = 2.713 %, GOF = 1.670.

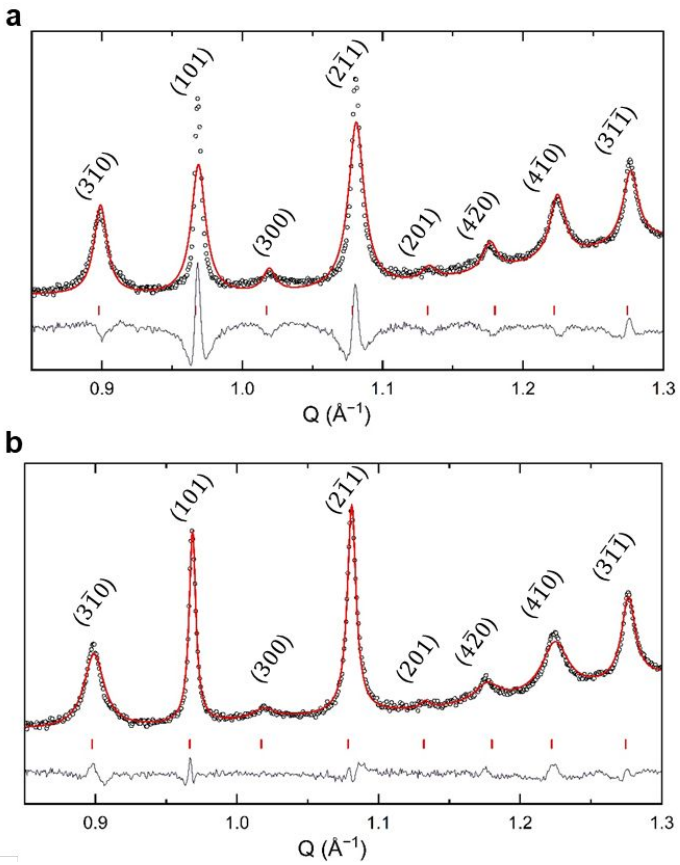

Figure S7. (a) Pawley fit using convolved Lorentzian and Gaussian size and strain models and (b) Pawley fit using Stephens parameters for *hkl*-dependent broadening.

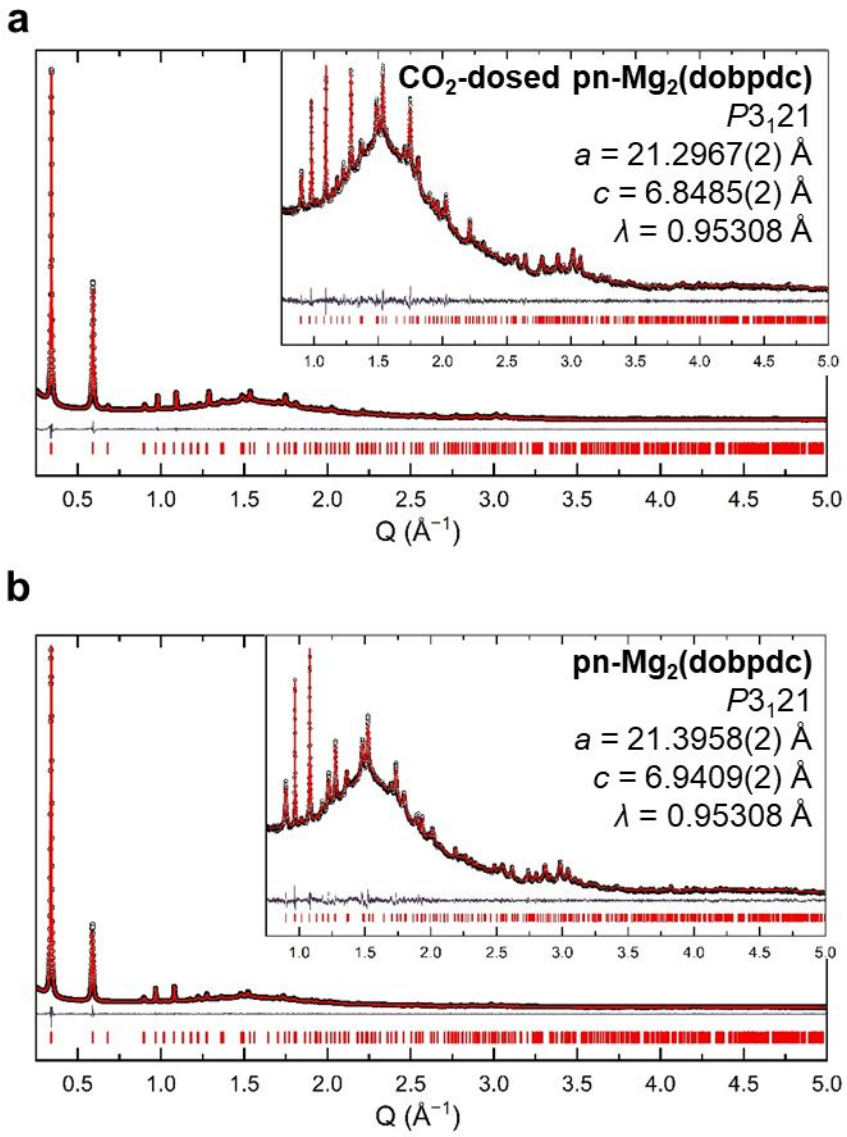

Figure S8. (a) Pawley fit of the powder X-ray diffraction pattern of CO_2-dosed pn-Mg_2(dobpdc) after activation under vacuum for 30 min, λ = 0.95308 Å**,** R_{wp} = 1.479 %, R_p = 1.064 %, R_{exp} = 0.782 %, GOF = 1.887. (b) Pawley fit of pn-Mg_2(dobpdc) after activation at 373 K for 1 h and then cooling to 298 K, λ = 0.95308 Å**,** R_{wp} = 1.799 %, R_p = 1.259 %, R_{exp} = 0.814 %, GOF = 2.196. Trigonal Stephens parameters were used to capture the *hkl*-dependent broadening effects in both materials.

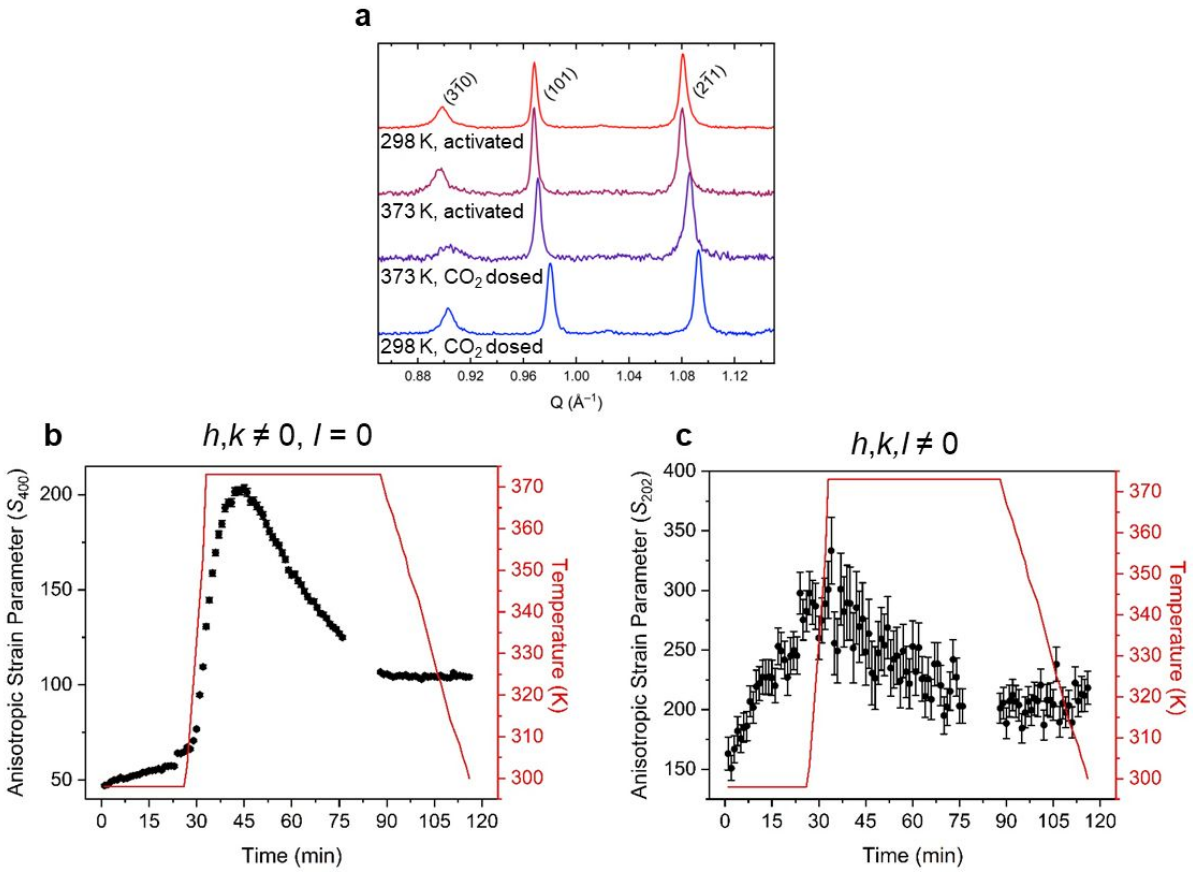

Figure S9. (a) Powder x-ray diffraction patterns of CO_2-dosed pn–Mg_2(dobpdc) collected under dynamic vacuum after equilibrating at 298 K for 30 min (blue pattern), heating to 373 K (purple pattern), equilibrating at 373 K for 1 h (burgundy pattern), and cooling to 298 K (red pattern). The Miller indices for each Bragg peak are denoted above the top pattern. (b) Evolution of the S_{400} parameter over time. The corresponding sample temperature is shown in red (right *y*-axis). (c) Evolution of the S_{202} parameter with time and temperature. Note that a small gap in the data between ≈ 75 and 85 minutes corresponds to a waited equilibration time during which no data were collected.

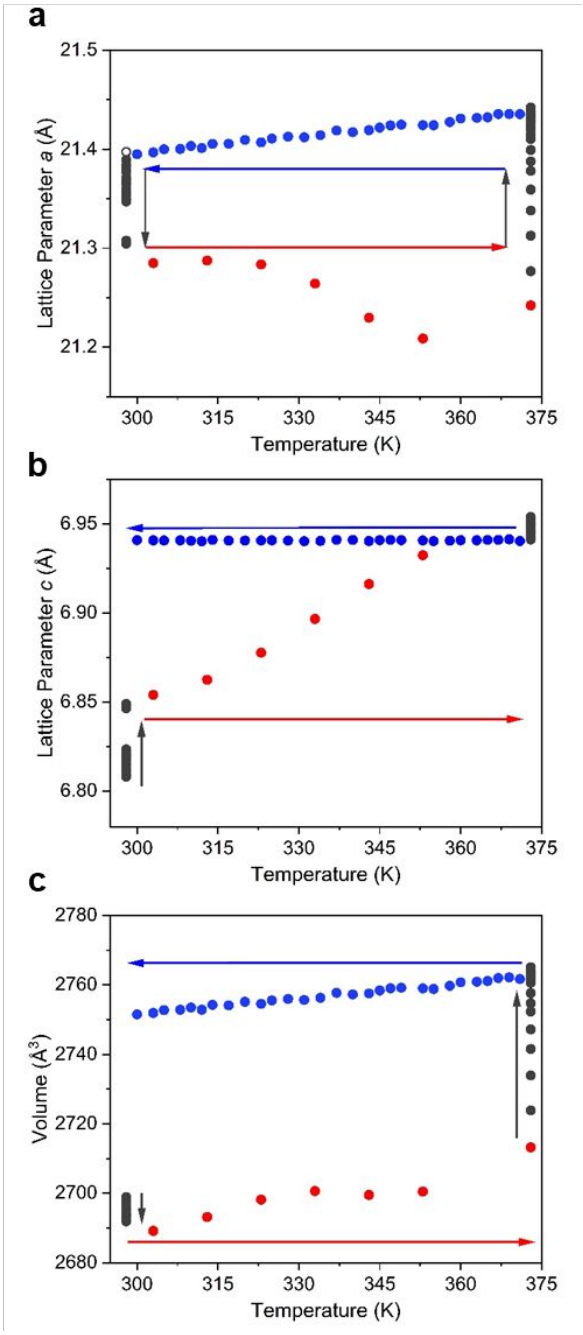

Figure S10. Lattice parameters (a) *a*, (b) *c*, (c) and volume for CO_2-dosed pn–Mg_2(dobpdc) during evacuation at 298 K under dynamic vacuum (gray data), heating to 373 K (red data), evacuation at 373 K (gray data) and cooling to 298 K (blue data). Symbols are larger than or commensurate with their error bars which represent $\pm 1\sigma$.

4. Supporting Infrared Scattering Scanning Near-Field Optical Microscopy Data

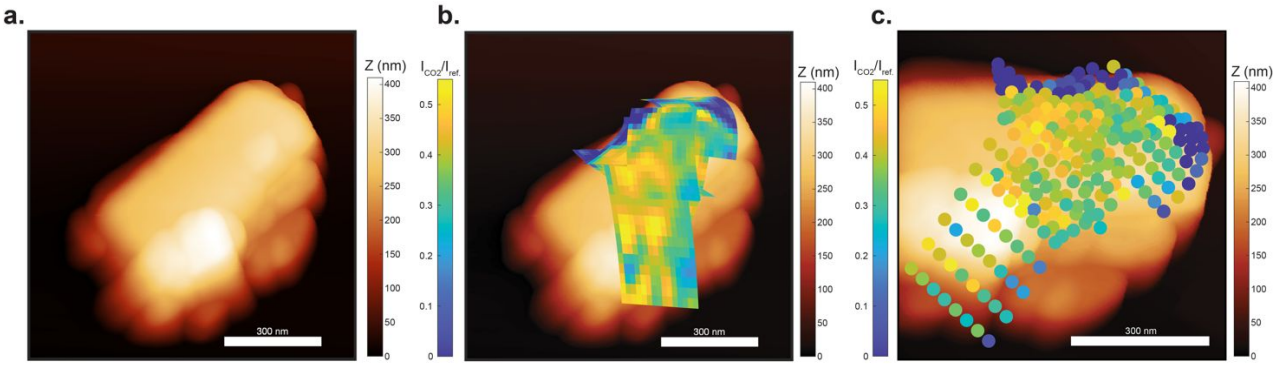

Figure S11. Additional IR *s*-SNOM measurement of pn–CO_2–Mg_2(dobpdc) mapping heterogeneity of chemisorbed CO_2 by a variation in the C–N stretching vibration at 1328 cm^{-1}. (a) AFM topography of additional measured crystals accompany nano FTIR imaging with relative intensity $I(_{\nu CO2})/ I(_{\nu ref})$ determined for each spectrum, represented (c) as points and (b) interpolated over the measured area.

5. Additional Characterization

5.1 Thermogravimetric Analysis (TGA)

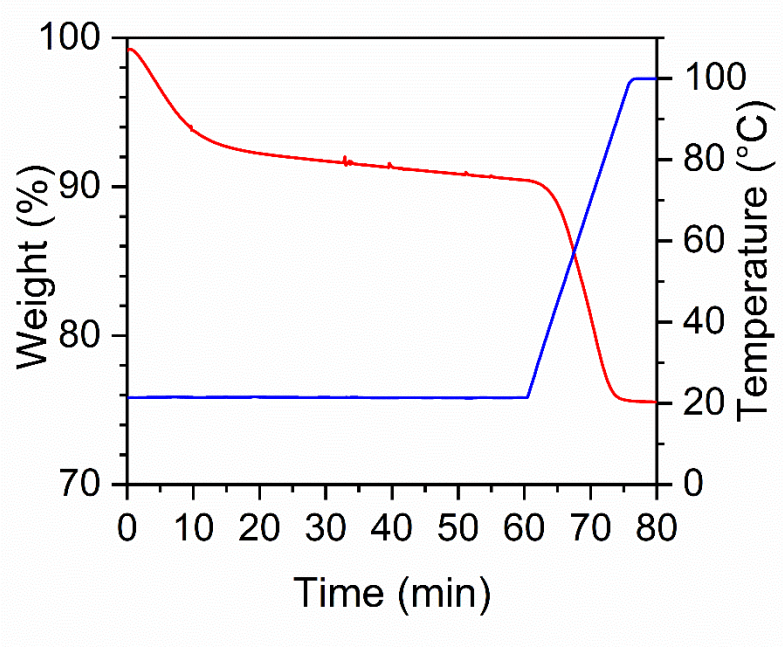

Figure S12. Thermogravimetric analysis trace of pn–CO_2–Mg_2(dobpdc) (also shown in Fig. 2d.) with corresponding temperature change.

5.2 Nuclear Magnetic Resonance (NMR) Spectrum

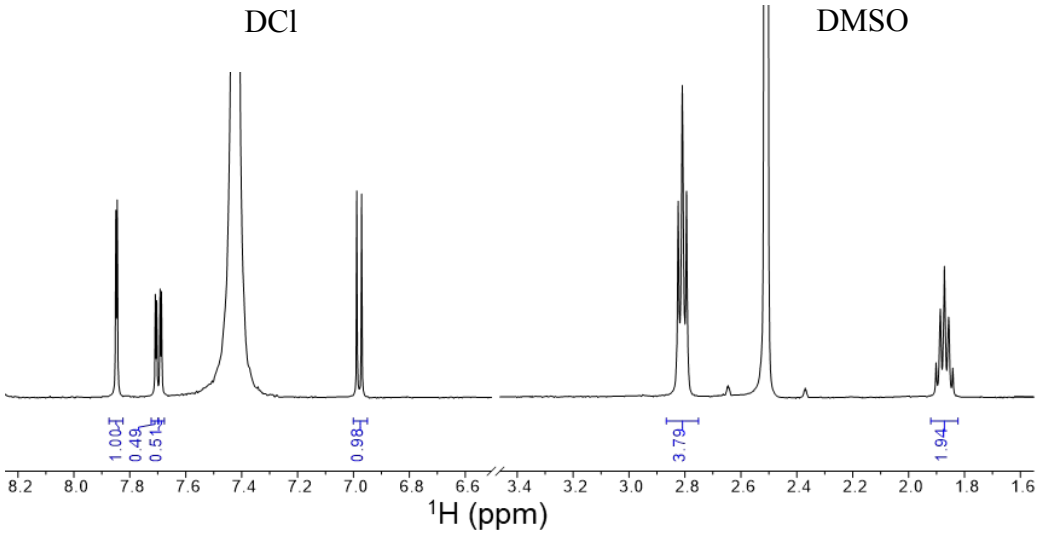

Figure S13. NMR spectrum (500 MHz) collected for a digested sample of pn–Mg_2(dobpdc) (dissolved in DCl/DMSO-d_6). The integration of the diamine resonances (δ = 1.87, 2.80 ppm) compared to the linker resonances (δ = 6.98, 7.70, 7.85 ppm) reveals ~95–98% amine appending. If the amine appending were to be 100%, then a ^{1}H ratio of 2:1 and 4:1 would be expected for the integration of the N–*H* resonance and C–*H* resonance, respectively, of the amine relative to the linker C–*H* resonance.

6. References

(1) Coelho, A. A. *TOPAS* and *TOPAS-Academic* : An Optimization Program Integrating Computer Algebra and Crystallographic Objects Written in C++. *J. Appl. Crystallogr.* **2018**, *51* (1), 210–218. https://doi.org/10.1107/S1600576718000183.

(2) Pawley, G. S. Unit-Cell Refinement from Powder Diffraction Scans. *J. Appl. Crystallogr.* **1981**, *14* (6), 357–361. https://doi.org/10.1107/S0021889881009618.

(3) McDonald, T. M.; Mason, J. A.; Kong, X.; Bloch, E. D.; Gygi, D.; Dani, A.; Crocellà, V.; Giordanino, F.; Odoh, S. O.; Drisdell, W. S.; Vlaisavljevich, B.; Dzubak, A. L.; Poloni, R.; Schnell, S. K.; Planas, N.; Lee, K.; Pascal, T.; Wan, L. F.; Prendergast, D.; Neaton, J. B.; Smit, B.; Kortright, J. B.; Gagliardi, L.; Bordiga, S.; Reimer, J. A.; Long, J. R. Cooperative Insertion of CO2 in Diamine-Appended Metal-Organic Frameworks. *Nature* **2015**, *519* (7543), 303–308. https://doi.org/10.1038/nature14327.

(4) Stephens, P. W. Phenomenological Model of Anisotropic Peak Broadening in Powder Diffraction. *J. Appl. Crystallogr.* **1999**, *32* (2), 281–289. https://doi.org/10.1107/S0021889898006001.

(5) Zhou, W.; Wu, H.; Yildirim, T.; Simpson, J. R.; Walker, A. R. H. Origin of the Exceptional Negative Thermal Expansion in Metal-Organic Framework-5 Zn 4 O (1 , 4 − Benzenedicarboxylate) 3. *Phys. Rev. B* **2008**, *78* (5), 054114. https://doi.org/10.1103/PhysRevB.78.054114.

(6) Huang, Z.; Willhammar, T.; Zou, X. Three-Dimensional Electron Diffraction for Porous Crystalline Materials: Structural Determination and Beyond. *Chem. Sci.* **2021**, *12* (4), 1206–1219. https://doi.org/10.1039/D0SC05731B.

(7) Biehler, E.; Pagola, S.; Stam, D.; Merkelbach, J.; Jandl, C.; Abdel-Fattah, T. M. A Comparison of Microcrystal Electron Diffraction and X-Ray Powder Diffraction for the Structural Analysis of Metal–Organic Frameworks. *J. Appl. Crystallogr.* **2025**, *58* (2), 398–411. https://doi.org/10.1107/S1600576724012068.

(8) Lee, J.-H.; Hyldgaard, P.; Neaton, J. B. An Assessment of Density Functionals for Predicting CO2 Adsorption in Diamine-Functionalized Metal–Organic Frameworks. *J. Chem. Phys.* **2022**, *156* (15), 154113. https://doi.org/10.1063/5.0084539.

(9) Forse, A. C.; Milner, P. J.; Lee, J.-H.; Redfearn, H. N.; Oktawiec, J.; Siegelman, R. L.; Martell, J. D.; Dinakar, B.; Zasada, L. B.; Gonzalez, M. I.; Neaton, J. B.; Long, J. R.; Reimer, J. A. Elucidating CO_2 Chemisorption in Diamine-Appended Metal–Organic Frameworks. *J. Am. Chem. Soc.* **2018**, *140* (51), 18016–18031. https://doi.org/10.1021/jacs.8b10203.

(10) Lee, J.-H.; Siegelman, R. L.; Maserati, L.; Rangel, T.; Helms, B. A.; Long, J. R.; Neaton, J. B. Enhancement of CO_2 Binding and Mechanical Properties upon Diamine Functionalization of M_2 (Dobpdc) Metal–Organic Frameworks. *Chem. Sci.* **2018**, *9* (23), 5197–5206. https://doi.org/10.1039/C7SC05217K.

(11) Siegelman, R. L.; Milner, P. J.; Forse, A. C.; Lee, J.-H.; Colwell, K. A.; Neaton, J. B.; Reimer, J. A.; Weston, S. C.; Long, J. R. Water Enables Efficient CO_2 Capture from Natural Gas Flue Emissions in an Oxidation-Resistant Diamine-Appended Metal–Organic Framework. *J. Am. Chem. Soc.* **2019**, *141* (33), 13171–13186. https://doi.org/10.1021/jacs.9b05567.

(12) Siegelman, R. L.; Thompson, J. A.; Mason, J. A.; McDonald, T. M.; Long, J. R. A Cooperative Adsorbent for the Switch-like Capture of Carbon Dioxide from Crude Natural Gas. *Chem. Sci.* **2022**, *13* (40), 11772–11784. https://doi.org/10.1039/D2SC03570G.